

# Oxide mediated spectral shifting in aluminum resonant optical antennas

Patrick M. Schwab,<sup>1,2</sup> Carola Moosmann,<sup>1</sup> Katja Dopf,<sup>1</sup> and Hans-Jürgen Eisler<sup>1,\*</sup>

<sup>1</sup>Light Technology Institute (LTI), Karlsruhe Institute of Technology, 76131 Karlsruhe, Germany

<sup>2</sup>Institute of Microstructure Technology (IMT), Karlsruhe Institute of Technology, 76344 Eggenstein-Leopoldshafen, Germany

\*[hans.eisler@kit.edu](mailto:hans.eisler@kit.edu)

**Abstract:** As a key feature among metals showing good plasmonic behavior, aluminum extends the spectrum of achievable plasmon resonances of optical antennas into the deep ultraviolet. Due to degradation, a native oxide layer gives rise to a metal-core/oxide-shell nanoparticle and influences the spectral resonance peak position. In this work, we examine the role of the underlying processes by applying numerical nanoantenna models that are experimentally not feasible. Finite-difference time-domain simulations are carried out for a large variety of elongated single-arm and two-arm gap nanoantennas. In a detailed analysis, which takes into account the varying surface-to-volume ratio, we show that the overall spectral shift toward longer wavelengths is mainly driven by the higher index surrounding material rather than by the decrease of the initial aluminum volume. In addition, we demonstrate experimentally that this shifting can be minimized by an all-inert fabrication and subsequent proof-of-concept encapsulation.

© 2015 Optical Society of America

**OCIS codes:** (250.5403) Plasmonics; (000.4430) Numerical approximation and analysis; (160.3900) Metals; (260.3060) Infrared; (260.7190) Ultraviolet; (290.5850) Scattering, particles.

---

## References and links

1. D. W. Pohl, "Near field optics seen as an antenna problem," in *Near-Field Optics: Principles and Applications*, M. Ohtsu and X. Zhu, eds. (World Scientific, Singapore, 2000), pp. 9–21.
2. P. Mühlischlegel, H.-J. Eisler, O. J. F. Martin, B. Hecht, and D. W. Pohl, "Resonant optical antennas," *Science* **308**, 1607–1609 (2005).
3. P. R. West, S. Ishii, G. V. Naik, N. K. Emani, V. M. Shalaev, and A. Boltasseva, "Searching for better plasmonic materials," *Laser Photonics Rev.* **4**, 795–808 (2010).
4. I. Zorić, M. Zäch, B. Kasemo, and C. Langhammer, "Gold, platinum, and aluminum nanodisk plasmons: Material independence, subradiance, and damping mechanisms," *ACS Nano* **5**, 2535–2546 (2011).
5. J. M. McMahon, G. C. Schatz, and S. K. Gray, "Ultraviolet plasmonics: the poor metals Al, Ga, In, Sn, Tl, Pb, and Bi," *Phys. Chem. Chem. Phys.* **15**, 5415–5423 (2013).
6. J. M. Sanz, D. Ortiz, R. Alcaraz De La Osa, J. M. Saiz, F. González, A. S. Brown, M. Losurdo, H. O. Everitt, and F. Moreno, "UV plasmonic behavior of various metal nanoparticles in the near- and far-field regimes: geometry and substrate effects," *J. Phys. Chem. C*, **117**, 19606–19615 (2013).
7. J. Aizpurua, G. W. Bryant, L. J. Richter, F. J. García De Abajo, B. K. Kelley, and T. Mallouk, "Optical properties of coupled metallic nanorods for field-enhanced spectroscopy," *Phys. Rev. B* **71**, 235420 (2005).
8. D. Smith, E. Shiles, and M. Inokuti, "The optical properties of metallic aluminum," in "Handbook of optical constants of solids," E. D. Palik, ed. (Academic Press, 1985).
9. H.-W. Liu, F.-C. Lin, S.-W. Lin, J.-Y. Wu, B.-T. Chou, K.-J. Lai, S.-D. Lin, and J.-S. Huang, "Single-crystalline aluminum nanostructures on a semiconducting GaAs substrate for ultraviolet to near-infrared plasmonics," *ACS Nano* **9**, 3875–3886 (2015).

10. M. W. Knight, L. Liu, Y. Wang, L. Brown, S. Mukherjee, N. S. King, H. O. Everitt, P. Nordlander, and N. J. Halas, "Aluminum plasmonic nanoantennas," *Nano Lett.* **12**, 6000–6004 (2012).
11. P. M. Schwab, C. Moosmann, M. D. Wissert, E. W.-G. Schmidt, K. S. Ilin, M. Siegel, U. Lemmer, and H.-J. Eisler, "Linear and nonlinear optical characterization of aluminum nanoantennas," *Nano Lett.* **13**, 1535–1540 (2013).
12. C. Langhammer, M. Schwind, B. Kasemo, and I. Zoric, "Localized surface plasmon resonances in aluminum nanodisks," *Nano Lett.* **8**, 1461–1471 (2008).
13. K. Thyagarajan, S. Rivier, A. Lovera, and O. J. F. Martin, "Enhanced second-harmonic generation from double resonant plasmonic antennae," *Opt. Express* **20**, 12860 (2012).
14. M. Rodriguez, C. Furse, J. S. Shumaker-Parry, and S. Blair, "Scaling the response of nanocrescent antennas into the ultraviolet," *ACS Photonics* **1**, 496–506 (2014).
15. V. Kochergin, L. Neely, C. Y. Jao, and H. D. Robinson, "Aluminum plasmonic nanostructures for improved absorption in organic photovoltaic devices," *Appl. Phys. Lett.* **98**, 133305 (2011).
16. N. P. Hylton, X. F. Li, V. Giannini, K.-H. Lee, N. J. Ekins-Daukes, J. Loo, D. Vercauteren, P. Van Dorpe, H. Sodabanlu, M. Sugiyama, and S. A. Maier, "Loss mitigation in plasmonic solar cells: aluminium nanoparticles for broadband photocurrent enhancements in GaAs photodiodes," *Sci. Rep.* **3**, 2874 (2013).
17. Q. Xu, F. Liu, Y. Liu, W. Meng, K. Cui, X. Feng, W. Zhang, and Y. Huang, "Aluminum plasmonic nanoparticles enhanced dye sensitized solar cells," *Opt. Express* **22**, A301–A310 (2014).
18. X. Jiao and S. Blair, "Optical antenna design for fluorescence enhancement in the ultraviolet," *Opt. Express* **20**, 29909–29922 (2012).
19. C. Forestiere, A. Handin, and L. Dal Negro, "Enhancement of molecular fluorescence in the UV spectral range using aluminum nanoantennas," *Plasmonics* **9**, 715–725 (2014).
20. K. B. Mogensen, M. Gühlke, J. Kneipp, S. Kadkhodazadeh, J. B. Wagner, M. Espina Palanco, H. Kneipp, and K. Kneipp, "Surface-enhanced Raman scattering on aluminum using near infrared and visible excitation," *Chem. Commun.* **50**, 3744–3746 (2014).
21. S. J. Tan, L. Zhang, D. Zhu, X. M. Goh, Y. Wang, K. Kumar, C.-W. Qiu, and J. K. W. Yang, "Plasmonic color palette for photorealistic printing with aluminum nanostructures," *Nano Lett.* **14**, 4023–4029 (2014).
22. J. Olson, A. Manjavacas, L. Liu, W.-S. Chang, B. Foerster, N. S. King, M. W. Knight, P. Nordlander, N. J. Halas, and S. Link, "Vivid, full-color aluminum plasmonic pixels," *Proc. Natl. Acad. Sci.* **111**, 14348–14353 (2014).
23. J. S. Clausen, E. Højlund-Nielsen, A. B. Christiansen, S. Yazdi, M. Grajower, H. Taha, U. Levy, A. Kristensen, and N. A. Mortensen, "Plasmonic metasurfaces for coloration of plastic consumer products," *Nano Lett.* **14**, 4499–4504 (2014).
24. M. W. Knight, N. S. King, L. Liu, H. O. Everitt, P. Nordlander, and N. J. Halas, "Aluminum for plasmonics," *ACS Nano* **8**, 834–840 (2014).
25. A. Taflove and S. C. Hagness, *Computational Electrodynamics: The Finite-Difference Time-Domain Method* (Artech House Publishers, 2004).
26. O. L. Muskens, V. Giannini, J. A. Sánchez-Gil, and J. Gómez Rivas, "Optical scattering resonances of single and coupled dimer plasmonic nanoantennas," *Opt. Express* **15**, 17736–46 (2007).
27. C. Moosmann, G. S. Sigurdsson, M. D. Wissert, K. Dopf, U. Lemmer, and H.-J. Eisler, "Investigating the influences of the precise manufactured shape of dipole nanoantennas on their optical properties," *Opt. Express* **21**, 594–604 (2013).
28. A. L. Ramaswamy and P. Kaste, "A Nanovision of the physiochemical phenomena occurring in nanoparticles of aluminum," *J. Energ. Mater.* **23**, 1–25 (2005).
29. S. K. Earl, D. E. Gómez, T. D. James, T. J. Davis, and A. Roberts, "Material effects on V-nanoantenna performance," *Nanoscale* **7**, 4179–4186 (2015).
30. A. Mohammadi, V. Sandoghdar, and M. Agio, "Gold, copper, silver and aluminum nanoantennas to enhance spontaneous emission," *J. Comput. Theor. Nanosci.* **6**, 2024–2030 (2009).
31. J. Zuloaga and P. Nordlander, "On the energy shift between near-field and far-field peak intensities in localized plasmon systems," *Nano Lett.* **11**, 1280–1283 (2011).

## 1. Introduction

The rapidly growing field of nanoplasmonics has a substantial impact on future optoelectronic devices. Resonant optical antennas play a major role as they offer the possibility of tuning and enhancing the light-matter interaction at the nanoscale [1, 2]. Over the last decade, metallic nanoparticles were investigated in detail as array or single entities to benefit from their potential as sub-wavelength devices. The main focus so far has been on the noble metals silver and gold. Both materials support resonance tuning from the infrared to the visible. However, gold suffers from a band edge: an interband transition occurs at approximately 2.4 eV, which corresponds to green light. Furthermore, the real part of the dielectric function of silver turns positive at about

3.8 eV, which prevents any plasmonic activity in the ultraviolet (UV) for silver. In addition, silver suffers from a rapid sulfidation. These circumstances promote gold as most frequently used plasmonic material due to its high stability and its biocompatibility especially for medical applications. From a manufacturing point of view, it allows for rather simple top-down as well as bottom-up approaches.

In recent times, however, aluminum has stimulated more and more interest and is therefore discussed amongst others, such as graphene, alloys or (post-)transition metals, as a promising candidate for future plasmonic devices [3–7]. Aluminum is one of the most abundant resources on earth and therefore seems to be a low cost alternative as plasmonic material. Three free electrons per atom result in a higher plasmon frequency compared to gold or silver, which enables (deep) UV plasmon enhanced applications [8]. Due to its complementary metal-oxide-semiconductor compatibility and the well known properties from bulk material, it is easily capable of being integrated into existing fabrication routines and therefore it is ready for mass production [9].

The potential of isolated aluminum rods in the UV regime was experimentally shown by Knight et al. [10] using cathodoluminescence, while the response of coupled and uncoupled antennas in the visible was investigated by conducting elastic and inelastic scattering experiments by our group [11]. Other antenna shapes for aluminum were investigated as well [12–14]. Recently, aluminum nanoparticles were investigated in typical plasmonic applications, i.e. efficiency enhancement in solar cells or photodetectors [15–17], fluorescence enhancement [18,19] or surface-enhanced Raman spectroscopy [20]. Aluminum was also shown to be a promising candidate for a pixelized color representation, which could find its way into display applications by exploiting the fact that aluminum plasmon resonances can cover the entire visible spectrum. Array arrangements can alter color and saturation and thereby allow for an RGB chromaticity [21–23].

As it is not one of the rare noble metals, aluminum undergoes an oxidation process. According to an X-ray photoelectron spectroscopy analysis on a thin film, a native oxide layer with a thickness of approximately 3 nm forms at the metal-air interface [12]. Knight et al. investigated how the conditions during the deposition of aluminum influence the optical response and proposed to use the spectral shift as a sensing element for the oxide content within the aluminum structure [24]. As the oxide layer is an inherent factor in the context of aluminum plasmonics, it is worth to gain a deeper insight in how it affects the behavior of aluminum nanostructures to be able to decide whether it makes sense to try to prevent this degradation process or to take it as an application-oriented material feature.

In this work, we present a systematic numerical study of how a nanoscale aluminum oxide shell influences the optical response of nanoantennas. We use finite-difference time-domain (FDTD) simulations [25] to investigate single aluminum rods and two-arm gap antennas, which are well-established representations of optical antennas inspired by the classical linear half-wave dipole antenna [26]. The examined resonances cover the optical regime from the UV to the near infrared. Our numerical approach allows us to discriminate between different modifications separately. These model structures go in detail beyond the experimentally available resonant optical antennas. Therefore, we analyze the concurrent roles of dielectric shell and changed metal core dimensions for structures that yield different surface-to-volume ratios. In the experimental section, we demonstrate how an inert environment during the sample preparation and a subsequent encapsulation in nitrogen atmosphere minimize degradation and consequential variations in the scattering response of the antennas. The encapsulation shields the aluminum from oxygen and water, enabling measurements in standard environments without complicated equipment and without changing the refractive index surrounding the antenna.

## 2. Simulations

To study the role of surface modification, the aluminum nanostructures were theoretically studied by using the commercially available simulation tool Lumerical FDTD Solutions ([www.lumerical.com](http://www.lumerical.com)), which is based on the finite-difference time-domain method to solve Maxwell's equations. A linearly polarized plane electromagnetic wave was incident on the optical antenna from the substrate side, which consisted of an infinitely extended glass substrate covered by a 50 nm indium tin oxide (ITO) layer. The polarization was chosen to be parallel to the antenna main axis, i.e. we used a longitudinal excitation throughout all our simulations. The antenna itself consisted of a single or two coupled aluminum bars for modeling the single-arm rod or coupled two-arm antenna structure, respectively. A schematic of the model used throughout this paper is given in Fig. 1. The height and width of the aluminum nanostructures were 30 nm unless otherwise specified in the text. The gap width of coupled two-arm antennas was fixed to 20 nm. To prevent numerical artifacts, i.e. unrealistic intense electric fields at the metallic edges and corners, these were modeled by a 3 nm radius of curvature. The surrounding oxide shell covering the metallic core at the metal-air interfaces was also rounded by the same radius.

We used tabulated data from Palik [8] to model the frequency dependent dielectric function of aluminum and its oxide and in-house data from ellipsometry measurements for the ITO layer within the frequency range of interest (see Appendix). A constant refractive index of  $n = 1.5$  was used for the glass substrate.

This model is an approximative and simplified approach to investigate the fundamental antenna behavior and how it is influenced during natural degradation at ambient conditions. We neither included the surface roughness, nor the exact realistic geometry, which is known to change the optical response and which can be deduced from scanning electron microscopy images and atomic force microscopy data [27], nor additional effects due to grain boundaries. Furthermore, we assumed a homogeneous oxidation and therefore a smooth oxide layer with constant thickness. The geometrical details are captured and depicted in Fig. 1.

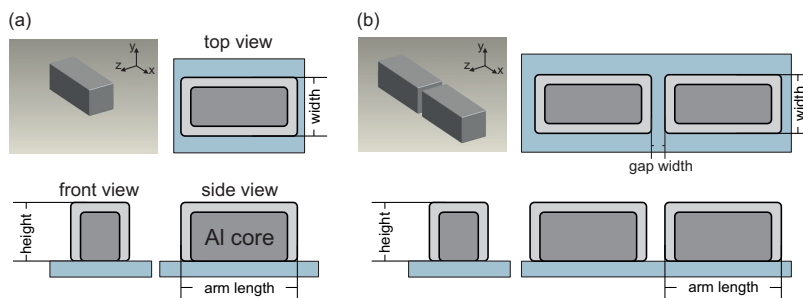


Fig. 1. Geometric model used for the numerical calculations of (a) a single-arm rod antenna and (b) a two-arm gap antenna with metallic core and oxide shell on an extended substrate. The geometric properties in the text refer to the sketch as indicated.

Within the total simulation volume of  $(1500 \text{ nm})^3$ , we used a finely resolved mesh with a spatial step size of 0.5 nm for the nanostructure and its close vicinity. The meshing became gradually coarser toward the outer boundaries, which consisted of a sufficient number of 24 perfectly matched layers (PML) to prevent any unwanted back reflection. The simulation time was 150 fs, which proved to be sufficiently high to achieve stable results after the decay of the excitation pulse. Extensive tests concerning the number of PMLs, the simulation time and the mesh size were carried out. Below a photon energy of 3.8 eV the mesh size of 0.5 nm was sufficiently small to achieve numerical convergence, while a meshing of 0.2 or 0.1 nm did not

change the qualitative and quantitative findings but, on the other hand, increased the required computational time drastically. To carry out reasonable simulations in the UV, i.e. above 3.8 eV the mesh size was decreased to 0.25 nm in order to prevent oscillations within a single mesh element.

The absorption and scattering cross sections were calculated by dividing the power flowing through the appropriate monitor boxes by the source intensity. The near-field intensity was given by the square of the electric field in the center of the antenna gap region of the two-arm gap antenna. Two-dimensional field representations in the  $xz$ -plane (*top view*) were extracted at half the antenna height.

### 3. Results and discussion

There has been quite some theoretical and experimental effort to investigate the role of oxidation [6, 12]. In the present work, we want to give a detailed insight to which extent dielectric and geometry modify the resonant behavior separately for differently shaped elongated optical antennas. First, we look at the far-field scattering response of single-arm antennas and how it is changed due to the presence of an oxide layer. To precisely distinguish between the geometric and the dielectric impact, we defined seven configurations, which are summarized in Table 1. This numerical approach exceeds the possibilities that are feasible with experiments. As long as not otherwise specified, we present the results for an oxide thickness of 3 nm, which is a valid assumption [28, 29]. Other thicknesses used in our simulations changed the results quantitatively but not qualitatively.

Table 1. Summary of the seven configurations used for the simulations.

no.	Description	Comment
I)	original aluminum volume	no oxide
II)	original aluminum volume	with oxide
III)	reduced aluminum volume	with oxide
IV)	reduced height, original length & width	no oxide
V)	reduced width, original length & height	no oxide
VI)	reduced length, original height & width	no oxide
VII)	reduced volume in all three dimensions	no oxide

Taking the oxide into account, we see a spectral red-shift in the antenna response. We select the representative structure of a 100 nm antenna to show exemplarily how the complete cross section spectrum is influenced by the different configurations. According to the calculated scattering cross sections depicted in Fig. 2(a), we conclude that for this specific antenna length the overall shift in the scattering response toward larger wavelengths is dominated by the oxide layer, which can be treated as a dielectric shell. The spectral red-shift caused by this change of the dielectric environment overcompensates the spectral blue-shift caused by the reduced aluminum volume. While a reduction in width and height both result in an increased aspect ratio and therefore in a slight spectral red-shift, the reduced length is the driving force for the blue-shift upon longitudinal excitation polarization, which is observed when the geometry is reduced in total volume.

As shown in Fig. 2(b), the spectral influence of both the reduction in aluminum volume and the additional oxide layer decreases with increasing antenna volume because the relative contribution from the surface diminishes. For the two largest antenna arm lengths under consideration, the aspect ratio is increased in such a way that the reduced volume even causes a slight spectral red-shift, which amplifies the effect of a resonance energy decrease from the dielectric. The outliers for arm lengths of 190 and 200 nm are a result of the interband damping at 1.5 eV.

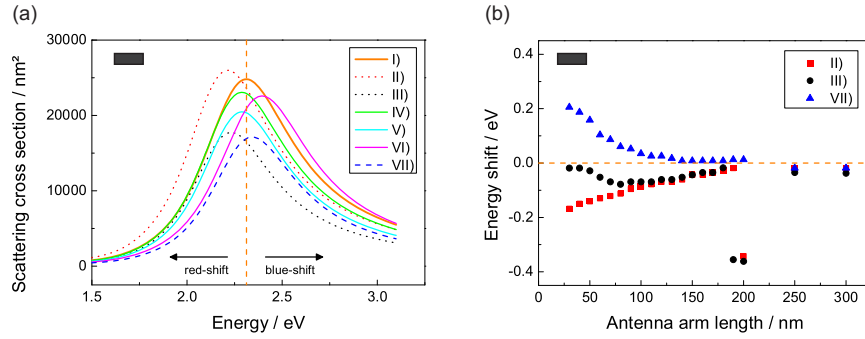


Fig. 2. (a) Calculated scattering cross sections for the seven configurations defined in Tab. 1 for a single-arm antenna. The nominal length is 100 nm, the width and height are 30 nm. The oxide thickness is 3 nm. (b) Calculated peak energy shift relative to the non-oxidized structures for different lengths. The vertical and horizontal orange dashed lines are guides to the eye and refer to the nominal peak energy of the original antenna before degradation.

This phenomenon is discussed in more detail for a variation of the oxide thickness later in the text.

The corresponding results for a coupled two-arm gap antenna with nominal gap width of 20 nm are depicted in Fig. 3. This antenna geometry exhibits the same general trends as presented for the uncoupled structures. The most important differences are due to the antenna gap, which acts as a coupling element. Here, we observe highly enhanced electric fields and therefore the question arises how the oxidation at this *hot-spot* region will change the resonance. Again, we see the influence from the interband transition for antenna arm lengths between 160 and 180 nm. For the largest two-arm gap antennas investigated in our simulations, the peak position shift because of the decrease in volume has nearly vanished. Therefore, the energetic shift is determined solely by the higher refractive index in the nanovicinity of the antenna as shown in Fig. 3(b).

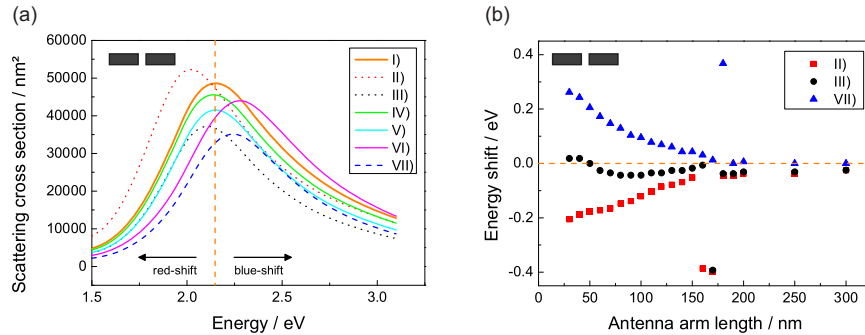


Fig. 3. (a) Calculated scattering cross sections for the seven configurations defined in Tab. 1 for a two-arm gap antenna. The nominal length is 100 nm, the width and height are 30 nm and the gap width is 20 nm. The oxide thickness is 3 nm. (b) Calculated peak energy shift relative to the non-oxidized structures for different lengths. The vertical and horizontal orange dashed lines are guides to the eye and refer to the nominal peak energy of the original antenna before degradation.

While the reduction in either width or height results in a less pronounced spectral red-shift for this antenna layout, the reduced longitudinal dimension has an increased influence on the

spectral position of the resonance peak.

The first observation is a direct consequence of the important role of the antenna gap and can also be seen in the gradient of peak energies in Fig. 4 where the growing oxide plays a larger role in the case of the single-arm antennas. This observation is in good agreement with numeric results from Mohammadi et al. [30] for copper nanostructures. The gap as coupling element perturbs the antenna dipole moment and thereby modifies the restoring force affecting the plasmon resonance. As a consequence, the gap prevails over and weakens the spectral shift induced by a change in aspect ratio.

The second observation, in contrast, is due to the fact that a growing oxide not only decreases the arm length but also increases the effective gap width, i.e. the distance between the metallic arms. Both modifications are known to blue-shift the antenna resonance [26]. Thus, when the length is reduced, two in principle independent effects sum up to this stronger increase in resonance energy compared to the case of a single-arm antenna.

By comparing the peak shifts in Figs. 2 and 3, we see that both observations lead to a stronger net blue-shift upon volume reduction (blue curve) while the presence of a higher dielectric in the gap region enhances the red-shift (red curve) compared to the single-arm antennas. To sum up, for the two-arm gap structures the influence from both the dielectric and the geometry is enhanced.

As aluminum has a strong interband transition at about 1.5 eV, scattering is damped in this energy regime. Therefore, no resonances emerge at this energy as can be seen in Figs. 4 and 5. As a consequence for antenna resonances close to this energy, the far-field response does not show a single but a dual-peak behavior because the main peak is suppressed. If we define the peak energy as the energy of the global maximum scattering intensity we will therefore not see a continuous but a semi-continuous shift. As an example, the inset in Fig. 4(a) illustrates the resulting difference in peak energy of about 0.3 eV between an unoxidized 200 nm single-arm antenna and the same antenna with a 1 nm oxide layer (blue triangle pointing down).

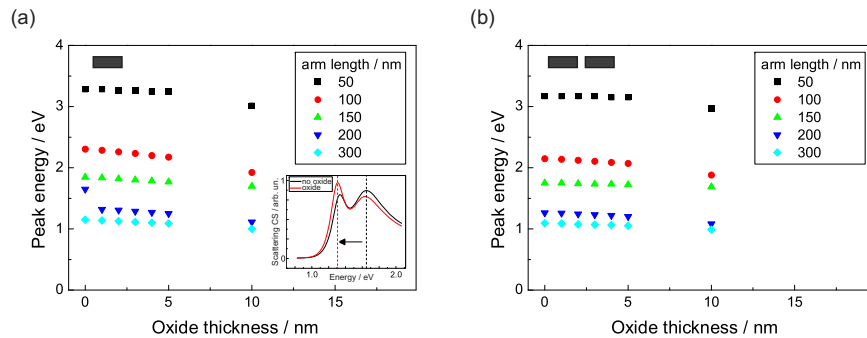


Fig. 4. Influence of the oxide thickness on the resonance peak position for (a) single-arm and (b) two-arm gap antennas of different arm lengths. The inset in (a) depicts the difference for a single-arm antenna with an arm length of 200 nm with (red) and without (black) a 1 nm oxide layer causing a jump in the peak energy as the main peak is suppressed by the interband absorption.

We introduce a weighting factor  $a$  that quantifies the influence of the reduction in volume (configuration VII,  $\Delta E_{VII}$ ) and the additional oxide (configuration II,  $\Delta E_{II}$ ) on the overall spectral shift (configuration III,  $\Delta E_{III}$ ) as follows:  $\Delta E_{VII} + a \cdot \Delta E_{II} = \Delta E_{III}$ . For both single-arm and two-arm gap antennas with resonances not influenced by the interband transition,  $a$  is always larger than 1 with  $1.08 \pm 0.05$  and  $1.17 \pm 0.08$ , respectively, which underlines the crucial role of the dielectric.

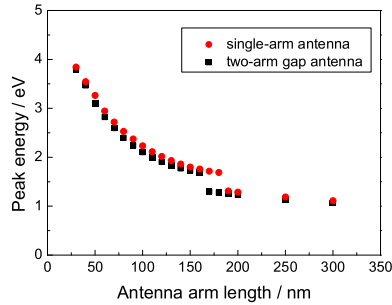


Fig. 5. Peak energy as a function of the antenna arm length. Resonances of two-arm gap antennas are slightly red-shifted compared to single-arm antennas due to the additional coupling. Single-arm and two-arm gap antenna resonances show an energetic gap around 1.5 eV due to the interband damping. Oxide thickness: 3 nm.

We also wanted to analyze the overall absorption as well as the near-field properties of an aluminum nanoantenna with and without an oxide layer. Therefore, in addition to the scattering cross section, we also investigated the absorption cross section and the intensity enhancement in the center of the antenna gap. In Fig. 6 we present the exemplary results for a 100 nm two-arm gap antenna, which are in good agreement with previously reported observations for single disks [12].

The spectral peak positions of both far-field and near-field properties of this structure shift toward lower energies when the structure is oxidized. As known from literature [31] the near-field maximum is found at a slightly lower energy compared to the far-field.

In the presence of an oxide layer, both the absolute peak absorption cross section and its integrated value are slightly increased for resonances well above the interband transition. Scattering as well as the local field enhancement are reduced in intensity. This result can be well reproduced with a simple metallic sphere covered by the oxide (data not shown). We also performed reference simulations without the underlying substrate (ITO and glass) to exclude additional effects arising from an index (mis)match of the upper oxide and the lower substrate, which define an insulator-metal-insulator (IMI) architecture. Even without the substrate, which shifts the overall response to lower energy, the increased absorption is still present.

In this context, we also looked at (i) the original metal volume but an increased gap width of 26 nm and (ii) the reduced metal volume but with the original gap width of 20 nm (data not shown) in order to further investigate the effects of reduced volume (configuration VII), which goes hand in hand with an increase in the gap distance.

The increased gap (i) not only blue-shifts the absorption and scattering resonance but leads to a slightly weaker response. In the other case (ii), the reduced volume with constant gap width also blue-shifts the peak. However, for the influence on the absolute cross section it has to be carefully differentiated between scattering and absorption: Scattering is reduced noticeably, while absorption is almost unchanged. According to Mie theory for spherical particles, scattering scales with the volume squared, while absorption increases linearly with the volume. In the presented case, the relative change in metal volume due to the oxide growth is in the order of 30 %. With a total length of (100+20+100) nm and the higher resonance energy of aluminum, the antenna can no longer be considered as a “small” particle in the quasi-static limit.

Finally, the additional dielectric shell alters scattering and absorption. Therefore, we also have to consider the polarizability  $\alpha$  as a function of the real and imaginary part of the dielectric function of aluminum and its oxide:  $\alpha$  relates directly to the scattering and absorption cross section with  $CS_{scat} \propto |\alpha|^2$  and  $CS_{abs} \propto \text{Im}\{\alpha\}$ , respectively. Thereby, we can calculate the

ratio between the cross sections for an embedded particle and a particle in vacuum. We see that the increase in the dielectric environment has a more pronounced impact on the absorption compared to the scattering. Thus, the absorption cross section of the oxidized structure is higher than for the unoxidized antenna, while scattering is lower. If we change the dielectric constant to a lower value (e.g. 1.46 for SiO<sub>2</sub>) it is possible to tune this behavior.

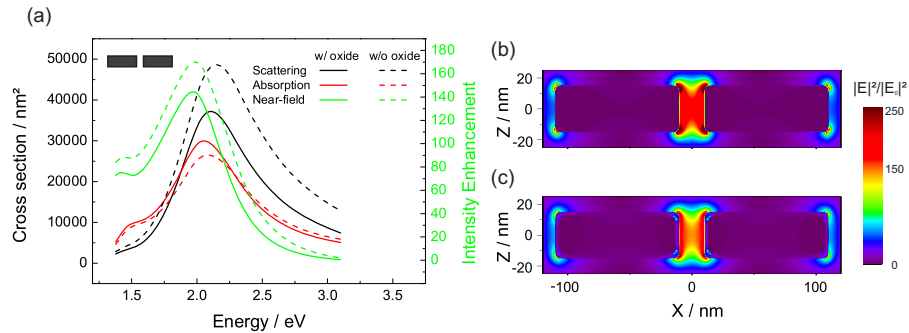


Fig. 6. (a) Scattering and absorption cross section as well as the near-field enhancement in the antenna gap for a two-arm gap antenna with (solid line) and without (dashed line) a 3 nm oxide layer. The nominal dimensions are: arm length 100 nm, gap width 20 nm, width and height 30 nm. Right: Normalized intensity distribution at resonance in the  $xz$ -plane (*top view*) at half the antenna height for the antenna (b) without and (c) with a 3 nm oxide layer covering the metallic core.

The corresponding normalized intensity distribution in the  $xz$ -plane for a coupled two-arm gap antenna is shown in Figs. 6(b) and 6(c). We see that the normalized near-field intensity  $I_{norm} = |E|^2/|E_0|^2$  decreases by more than 15 % in the presence of an oxide layer. The spatial distribution remains almost the same as the electric field is still mainly localized at the antenna gap and not concentrated in the higher index oxide layer, which acts as a screening layer for the evanescent electric field.

#### Sample fabrication and dark-field scattering spectroscopy

To prepare the samples used for the experiments presented in the following, we used a standard glass cover slip with a conductive 50 nm ITO layer for electron-beam lithography. The sample was treated thermally to reduce surface roughness and auto-fluorescence and to increase conductivity and transmission. A diluted PMMA 950k resist with a resulting thickness of about 60 nm was exposed at 10 kV. After exposure and development, a 30 nm thick aluminum film was thermally evaporated and finally a lift-off process was performed. For encapsulation, we used a second glass cover, a metallic fitting for the microscope and a UV curable glue (Norland NOA68, www.norlandprod.com) such that the nanostructures were finally protected from oxygen and water by a gap filled with nitrogen. All these steps were performed in nitrogen atmosphere inside a glovebox. In contrast to passivating the aluminum with a protective layer, this approach does not disturb the local dielectric environment. To our knowledge, this is the first time that such a step, which is widely spread in other fields of optoelectronics, was applied for the protection of optical antennas.

Linear scattering spectroscopy mediated by dark-field microscopy was used to optically characterize the time-integrated far-field response. We used an inverted microscope (Zeiss Axio Observer) with a halogen light source and a dark-field condenser in combination with a grating based spectrometer (Princeton Instruments Acton SpectraPro 2500i) with an attached electron multiplying charge-coupled device camera (Andor iXon) to obtain individual scattering spectra

from single nanoantennas. The spectra were normalized on the background with respect to the source and the system function (see Appendix). We fitted a first order Lorentzian to the measured data in order to derive the spectral peak position of each individual antenna spectrum. Figure 7 depicts the temporal behavior of the scattering peak position for both the encapsulated and the non-encapsulated sample. We limited ourselves to a 100 nm two-arm gap antenna to avoid influences from the interband transition. On both samples, we characterized the same antenna at different points in time in order to exclude effects of geometry variation within each set of measurements. We see that the spectral peak position remains constant for the encapsulated device, while the resonance spectrum for the sample fabricated and stored in ambient conditions shifts toward lower energy. After approximately three weeks of observation, the peak energy approaches a lower threshold indicating the self-terminating character of the oxidation process. Directly after the fabrication, we observe an energetic gap between both samples. This might arise from the beginning environmental impact. Furthermore, we cannot exclude initial differences between both structures arising from the fabrication process. The resonance energy decrease is larger than what was shown by Langhammer et al. who investigated experimentally a different geometry by a different spectroscopic approach [12]. Assuming a linear peak energy dependence on the oxide thickness as given by Fig. 4(b), the here observed spectral shift corresponds to an oxide growth of below 5 nm between the initial and the final measurement. By simply comparing values from optical characterization measurements with numerics we thus obtain a reasonable estimate of the oxide thickness. We speculate that the actual oxide thickness might also differ depending on the resulting surface roughness.

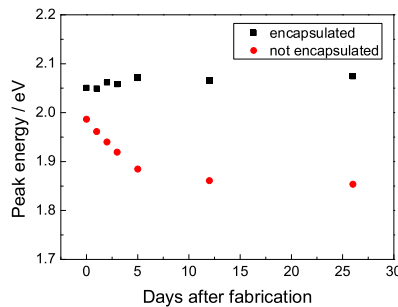


Fig. 7. Peak position shifting as a function of time for an encapsulated and a non-encapsulated aluminum two-arm gap antenna with an arm length of 100 nm. While the peak energy remains constant for the encapsulated sample, there is a noticeable peak shift for the non-encapsulated sample.

#### 4. Conclusion

In this work, we investigated the influence of a growing oxide layer covering a shrinking metallic core for aluminum resonant optical antennas. We used the finite-difference time-domain method to determine the individual impact of a dielectric shell and a variation of geometric parameters of the metallic core. We wanted to point out how opposing trends finally sum up and that they might be included in design considerations for optical applications throughout the entire spectrum from the UV to the NIR. For the majority of structures, we see that the volume reduction leads to a spectral blue-shift, whereas the higher index oxide in the close vicinity of the metal overcompensates this and finally leads to an overall red-shift of the antenna response. The relative contribution from individual modifications differs as a function of surface-to-volume ratio. Although the individual spectral shifting from opposing mechanisms is enhanced compared to single-arm structures due to the high local field in the gap region, a

comparison between single-arm and two-arm gap antennas shows that the growing distance between adjacent arms decreases the coupling strength and therefore reduces the overall red-shift.

In addition to these numerical results, we have experimentally shown that a strictly inert fabrication together with an encapsulation can prevent aluminum optical antennas from degradation. There is a clear qualitative trend toward a stable peak resonance for the encapsulated sample, whereas the sample stored at ambient conditions shows a spectral shift over time.

### Appendix: Dielectric constant of ITO and dark-field spectra

In Fig. 8 we show the dielectric function of ITO used for the FDTD simulations. The dark-field spectra from the encapsulated and non-encapsulated samples are depicted in Fig. 9.

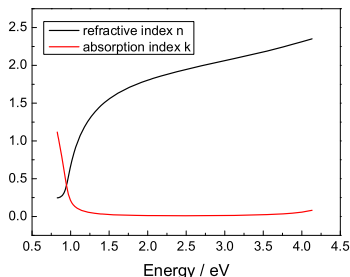


Fig. 8. Refractive index  $n$  and absorption index  $k$  for ITO as measured by ellipsometry.

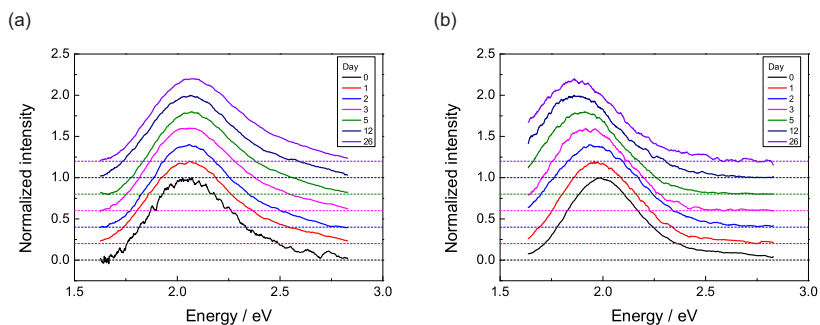


Fig. 9. Dark-field spectra of (a) an encapsulated (b) and a non-encapsulated aluminum two-arm gap antenna with a nominal arm length of 100 nm. All spectra have been normalized to unity and an offset of 0.2 has been introduced between individual spectra to facilitate discrimination. The horizontal dashed lines are guides to the eye. The standard deviation for the encapsulated sample is below 2.8 nm, which is in good accordance with the measurement uncertainty. Different signal-to-noise ratios arise from slight differences in the alignment between condenser and sample during individual measurements.

### Acknowledgments

The authors gratefully acknowledge continuous support by Prof. U. Lemmer from the Light Technology Institute (LTI), KIT and Prof. M. Siegel and Dr. K. Illin from the Institute of Micro- und Nanoelectronic Systems (IMS), KIT. Furthermore, we acknowledge support by the Karlsruhe School of Optics and Photonics (KSOP) and the Helmholtz International Research School for Teratronics (HIRST). We acknowledge support by Deutsche Forschungsgemeinschaft and Open Access Publishing Fund of Karlsruhe Institute of Technology.